Support Information

Zero Thermal Expansion in High-Entropy Molybdate

Xin Chen[1#], Hao Li[2#], Qingjie Wang[1], Kaiyue Zhao[1], Gongshen He[3], Yongqiang Qiao[1*], Qilong Gao[1*], Shogo Kawaguchi[4], Bingbing Fan[3*], Rui Zhang[3], and Jun Chen[2,5]

[1]School of Physics, Zhengzhou University, Zhengzhou 450001, China

[2]State Key Laboratory of Tropic Ocean Engineering Materials and Materials Evaluation, Hainan University, Haikou 570228, China

[3]School of Material Science and Engineering, Zhengzhou University, Zhengzhou, 450001, China

for Advanced Studies in Precision Instruments, Hainan University, Haikou, 570228 China

[4]Japan Synchrotron Radiation Research Institute (JASRI), Sayo-cho, Hyogo 679-5198, Japan

[5]Department of Physical Chemistry, Beijing Advanced Innovation Center for Materials Genome Engineering, University of Science and Technology Beijing, Beijing 100083, China

**To whom correspondence should be addressed. Email:* yongqiangqiao@zzu.edu.cn (Y. Qiao) *qilonggao@zzu.edu.cn(Q. Gao); fanbingbing@zzu.edu.cn (B. Fan)*

Supplementary Information Contents

1 Experiment and Characterization

1.1 Experiment

The high-entropy oxide ceramic KMHO was synthesized via the solid-state sintering method. The raw materials included K_2CO_3 (West Asia, 99%), MnO (Aladdin, 99%), In_2O_3 (West Asia, 99.99%), Sc_2O_3 (HWRK, 99.99%), Lu_2O_3 (Macklin, 99.99%), Yb_2O_3 (Macklin, 99.99%), and MoO_3 (West Asia, 99.95%). All raw materials were weighed according to their stoichiometric molar ratios and thoroughly mixed in an agate mortar with an appropriate amount of anhydrous ethanol as a milling medium. The mixture was ground for 2 hours to ensure homogeneous dispersion and fine particle size. To mitigate the adverse effect of CO_2 release from K_2CO_3 decomposition during high-temperature sintering on the sample densification, the mixed powder was pre-calcined in an alumina crucible at 600 °C for 6 hours in a muffle furnace. The pre-calcined powder was then reground in an agate mortar with anhydrous ethanol for another 2 hours. The resulting fine powder was uniaxially pressed into cylindrical pellets (Φ8 × 5 mm) under a pressure of 2 MPa. Finally, the green compacts were sintered at 750 °C for 10 hours in a muffle furnace, followed by furnace cooling to room temperature, yielding the target high-entropy oxide ceramic samples.

1.2 Characterization

The phase purity of the sample was examined using high-resolution synchrotron X-ray diffraction at the BL02B2 beamline. A two-dimensional detector (XRD3025) was used to collect powder diffraction data. Automated data collection was carried out with temperature control using LabVIEWTM software along with high and low temperature nitrogen gas flow systems. The set temperature range was from 300 to 1000 K, a temperature rate of 30 K/min, and a thermal equilibration delay of 3 min. The diffraction patterns were refined by the Rietveld method using the FullProf software to obtain detailed information on the crystal structure, lattice parameters, and interatomic distances. Raman spectra were collected on a Horiba Jobin Yvon LabRAM HR spectrometer with a 532 nm excitation wavelength. The microstructure of the sample

was characterized using a scanning electron microscope (Zeiss/Auriga FIB) and a transmission electron microscope (FEI Talos F200S), while the elemental composition and spatial distribution were analyzed by energy-dispersive X-ray spectroscopy (EDS). X-ray photoelectron spectroscopy (XPS) measurements were performed on an Escalab 250Xi spectrometer equipped with an Al Kα radiation source, and the binding energies were calibrated against the C 1s peak at 284.8 eV. Thermal analyses, including differential scanning calorimetry (DSC) and thermogravimetric analysis (TGA), were conducted on a TA449F3 system over a temperature range from room temperature to 900 K at a heating rate of 10 K/min. The ionic conductivity was measured using a CHI650E electrochemical workstation. Additionally, the UV–Vis absorption spectrum of the sample was recorded using a TU-1901 double-beam UV–Vis spectrophotometer.

1.3 Computational detail

First-principles calculations based on density-functional theory (DFT) are carried out using the Vienna ab initio simulation package (VASP).[1] The exchange and correlation effects were included within the Perdew-Burke-Ernzerhof (PBE) generalized gradient approximation (GGA).[2] The interaction between the atomic core and valence electrons is described using pseudopotentials based on the projector augmented plane wave (PAW) method.[3]

1.4 The calculation of CTE

The coefficient of thermal expansion (CTE) is a key parameter characterizing the thermal expansion behavior of materials. It reflects the relative change in the unit length or unit volume of a material per 1 K temperature variation under constant pressure conditions, which corresponds to the linear thermal expansion coefficient (α_l) and the volumetric thermal expansion coefficient (α_V), respectively. Their expressions are defined as follows:

$$\alpha_l = \frac{l\text{-}l_0}{l_0(T\text{-}T_0)} = \frac{\Delta l}{l_0 \Delta T} \tag{1}$$

$$\alpha_V = \frac{V - V_0}{V_0 (T - T_0)} = \frac{\Delta V}{V_0 \Delta T} \tag{2}$$

where l_0 and V_0 denote the initial length and volume at T_0; l and V represent its length and volume at T; and ΔT refers to the temperature variation.

2 Figures and tables

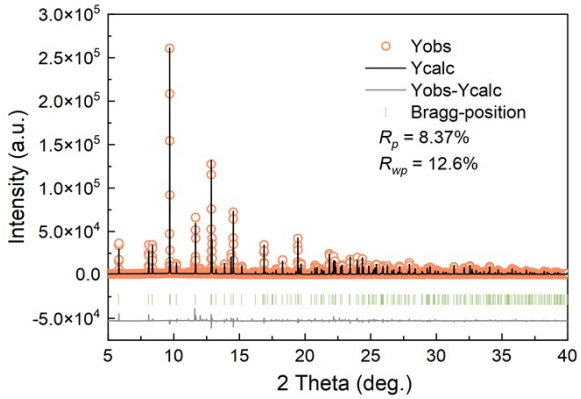

Fig. S1 Rietveld refinement pattern of KMHO at room temperature

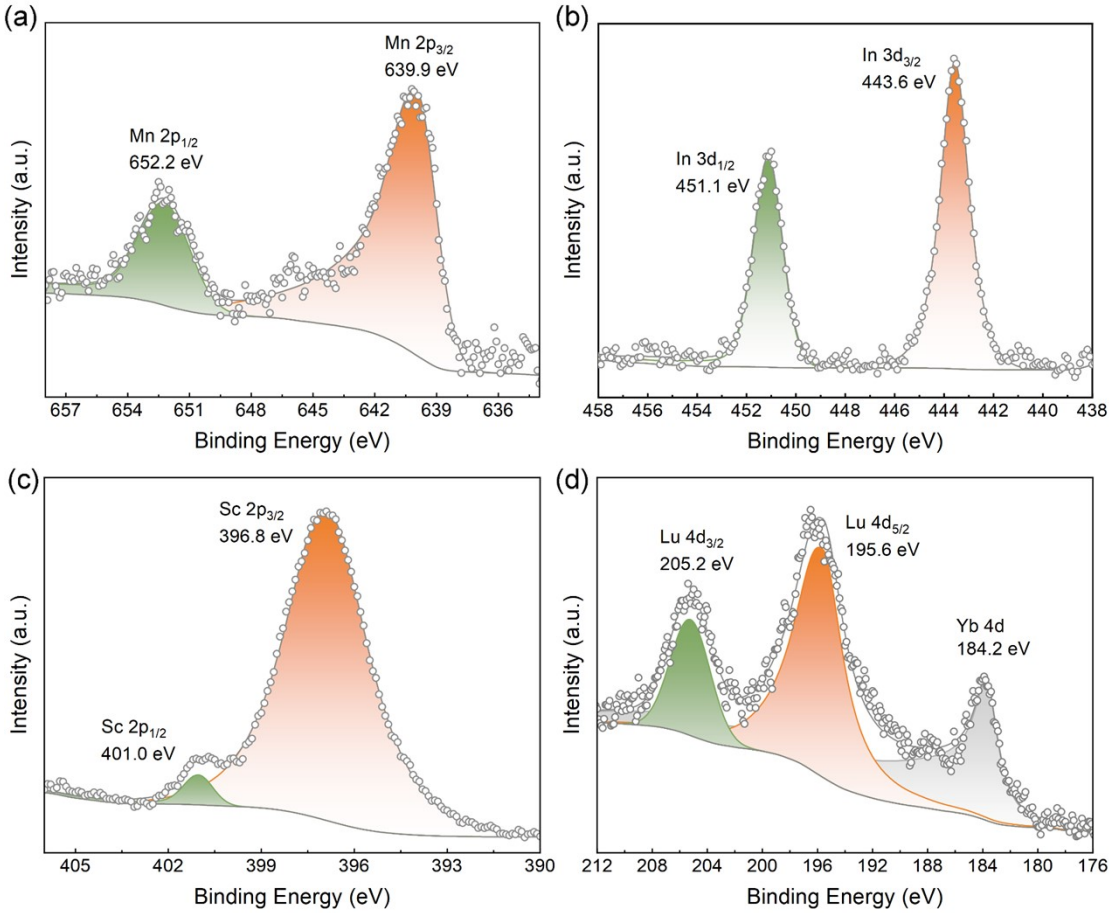

Figure S2. High-resolution XPS spectra of (a) Mn 2p, (b) In 3d, (c) Sc 2p, (d) Lu 4d, and Yb 4d in KMHO.

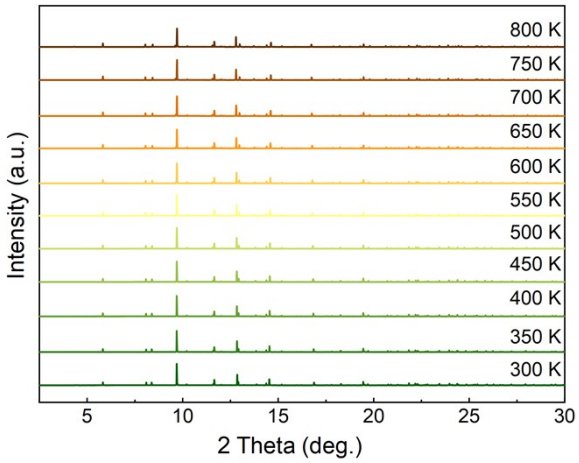

Figure S3. Variable temperature XRD patterns of KMHO.

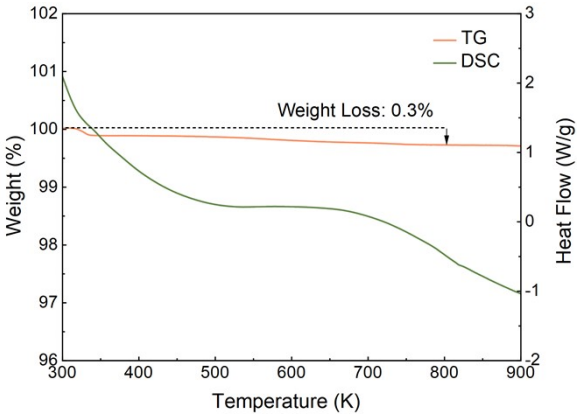

Figure S4. TG and DSC curves of KMHO.

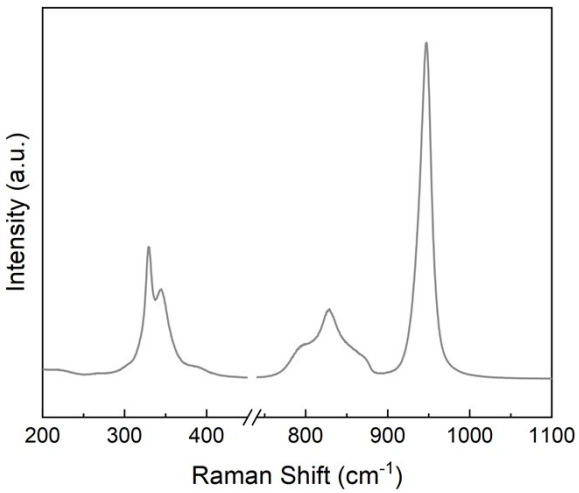

Figure S5. Unpolarized Raman spectrum of KMHO at room temperature.

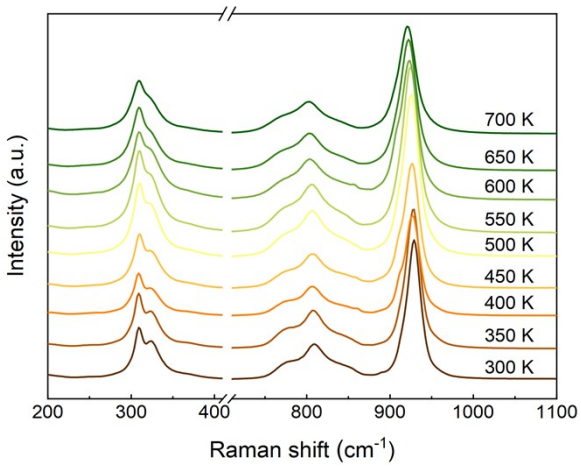

Figure S6. Variable Raman spectroscopy of KMHO.

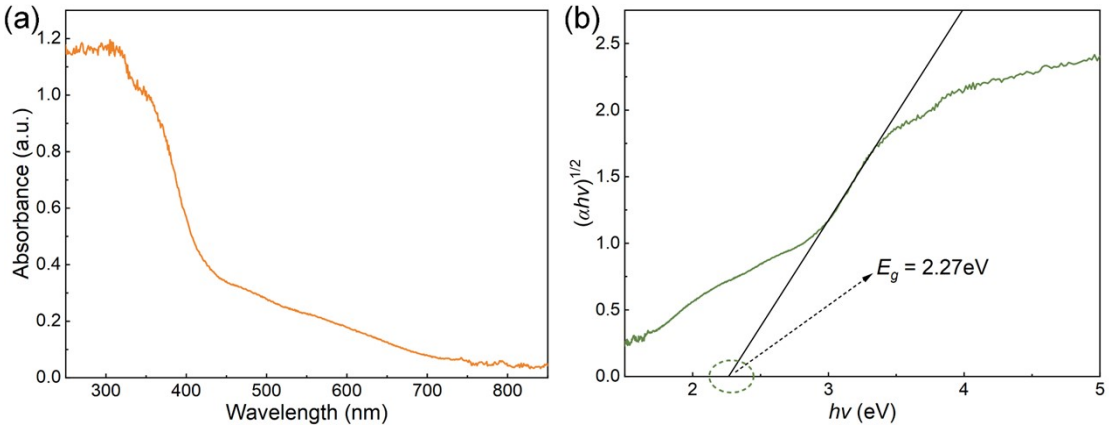

Figure S7. (a) UV-visible absorption spectra of KMHO, (b) schematic diagram of band gap calculated from UV-vis absorption spectroscopy.

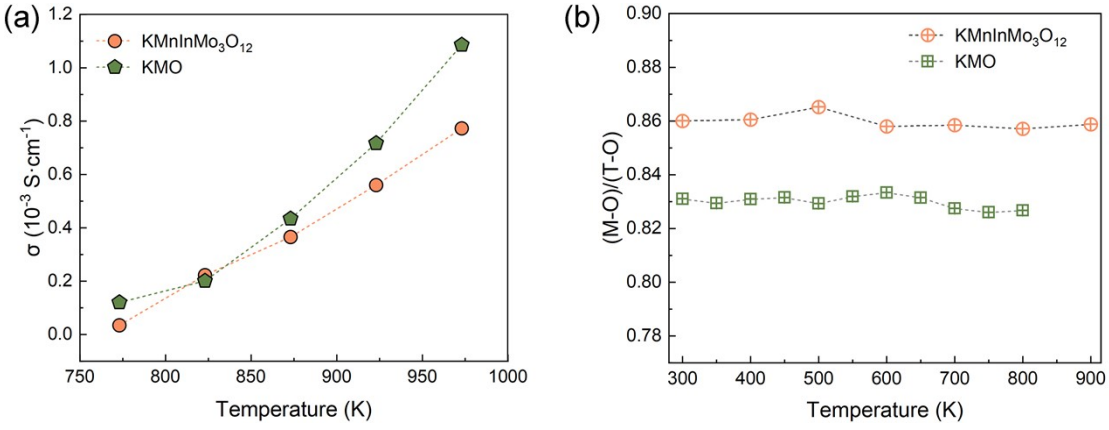

Figure S8. (a) Temperature dependence of the ionic conductivity for KMHO and $KMnInMo_3O_{12}$, (b) temperature dependence of the (M–O)/(T–O) ratios for KMHO and $KMnInMo_3O_{12}$.

Table S1. The optimal Rietveld refined structure parameters of KMHO at 300 K.

Atom	Occ	x	y	z	B_{iso} (Å^3)
K	1	0	0	0	4.00438(13)
Mn	1	0	0	0.14323(7)	0.08098(8)
Sc	0.25	0	0	0.14323(7)	0.08098(8)
In	0.25	0	0	0.14323(7)	0.08098(8)
Lu	0.25	0	0	0.14323(7)	0.08098(8)
Yb	0.25	0	0	0.14323(7)	0.08098(8)
Mo1	1	0.28491(19)	0	0.25000(0)	0.89834(9)
Mo2	1	0.28491(19)	0	0.25000(0)	0.89834(9)
Mo3	1	0.28491(19)	0	0.25000(0)	0.89834(9)
O1	1	0.02508(19)	0.19307(13)	0.19196(18)	1.14800(11)
O2	1	0.02508(19)	0.19307(13)	0.19196(18)	1.14800(11)
O3	1	0.02508(19)	0.19307(13)	0.19196(18)	1.14800(11)
O4	1	0.02508(19)	0.19307(13)	0.19196(18)	1.14800(11)
O5	1	0.02508(19)	0.19307(13)	0.19196(18)	1.14800(11)
O6	1	0.02508(19)	0.19307(13)	0.19196(18)	1.14800(11)
O7	1	0.18846(18)	0.16002(12)	0.09029(18)	1.60449(10)
O8	1	0.18846(18)	0.16002(12)	0.09029(18)	1.60449(10)
O9	1	0.18846(18)	0.16002(12)	0.09029(18)	1.60449(10)
O10	1	0.18846(18)	0.16002(12)	0.09029(18)	1.60449(10)
O11	1	0.18846(18)	0.16002(12)	0.09029(18)	1.60449(10)
O12	1	0.18846(18)	0.16002(12)	0.09029(18)	1.60449(10)

Table S2. Variation of unit cell parameters, unit cell volume, R_p, and R_{wp} with Temperature.

Temperature (K)	Lattice parameters			R_p (%)	R_{wp} (%)
	a/b (Å)	*c* (Å)	*v* (Å^3)		
300	9.58909	24.78824	1973.488	8.37	12.6
350	9.58331	24.81729	1973.443	9.18	13.6
400	9.57708	24.84411	1973.414	8.40	12.5
450	9.5714	24.87278	1973.358	8.98	13.1
500	9.5656	24.90331	1973.384	8.56	12.7
550	9.55999	24.93303	1973.424	8.81	13.1
600	9.55429	24.96426	1973.54	8.62	12.9
650	9.54841	24.99806	1973.781	9.42	14.0
700	9.54318	25.02848	1974.018	9.65	14.3
750	9.5381	25.0589	1974.314	9.05	13.4
800	9.5333	25.08738	1974.569	10.50	15.9

Table S3. CTE and temperature range of some typical ZTE materials

Materials	α_v (10^{-6} K^{-1})	Temperature range (K)	Ref.
$LaFe_{10.1}Cu_{0.5}Si_{2.4}$	0.84	185-250	4
$CrVMoO_7$	-1.92	100-240	5
$Hf_{0.85}Ta_{0.15}Fe_2C_{0.01}$	2.40	85-245	6
$Mn_3Fe_{0.2}Co_{0.2}Ni_{0.2}Mn_{0.2}Cu_{0.2}N$	0.72	10-180	7
β-$Cu_2V_2O_7$	-2.70	153-323	8
$Gd_{0.25}Dy_{0.75}Co_{1.93}Fe_{0.07}$	0.48	10-275	9
$K_{0.5}Bi_{0.5}TiO_3$	1.30	373-573	10
$Cs_{0.7}Ni[Fe(CN)_6]_{0.9}\cdot 2.9H_2O$	-1.20	100-300	11
ReO_3	-1.90	2-220	12
$CoHfF_6$	1.99	350-573	13
$N(CH_3)_4CuZn(CN)_4$	2.01	218-368	14
$Sc_{0.725}Nb_{0.275}Fe_2$	2.07	108-264	15
$Ho_2Fe_{16}Cr$	1.29	13-330	16
$Hf_{0.6}Ti_{0.4}Fe_{2.5}$	1.59	100-450	17
$TaPO_5$	-1.70	473-873	18
KMHO	1.53	300-800	This work

Table S4. The ADP values of O1 and O7 at 300-800 K.

Atom	O1-11	O1-22	O1-33	O2-11	O2-22	O2-33
300	0.00488(14)	0.00522(13)	4.4E-4(1)	0.00401(13)	0.00388(13)	6.7E-4(1)
350	0.00543(15)	0.00502(14)	6.3E-4(1)	0.00467(13)	0.00439(13)	9.2E-4(2)
400	0.00540(15)	0.00500(15)	7.4E-4(2)	0.00498(14)	0.0045(14)	7.4E-4(2)
450	0.00664(16)	0.00603(16)	5.8E-4(2)	0.00775(18)	0.00568(16)	8.9E-4(2)
500	0.00852(17)	0.00594(16)	7.1E-4(2)	0.00805(16)	0.00558(16)	9.8E-4(2)
550	0.01025(19)	0.00585(17)	9.9E-4(2)	0.0081(17)	0.00699(17)	0.00104(2)
600	0.01144(19)	0.00622(17)	0.00109(2)	0.00844(17)	0.00804(18)	0.00100(1)
650	0.01304(22)	0.00748(19)	0.00106(2)	0.01113(19)	0.00907(19)	0.00114(2)
700	0.0135(22)	0.00897(20)	0.00109(2)	0.01182(20)	0.01094(21)	0.00126(2)
750	0.01383(23)	0.00955(21)	0.00113(2)	0.01401(21)	0.01289(22)	0.00164(3)
800	0.01582(30)	0.01027(26)	0.00136(3)	0.01708(30)	0.01634(31)	0.00184(3)

Table S6. The variation of Raman Shift with pressure.

Pressure (GPa)	Raman Shift (cm^{-1})
0	345.27662
0.25	345.19655
0.47	344.9409
0.71	344.75403
1.02	344.30328
1.37	343.58024
1.65	342.1728
2.14	341.87765
2.70	340.69088
3.00	340.5041

Reference

1 G. Kresse, and J. Furthmuller, Efficient iterative schemes for ab initio total-energy calculations using a plane-wave basis set. *Phys. Rev. B,* 1996, **54** (16), 11169-11186.

2 J. P. Perdew, K. Burke, and M. Ernzerhof, Generalized gradient approximation made simple. *Phys. Rev. Lett.,* 1996, **77** (18), 3865-3868.

3 G. Kresse, and D. Joubert, From ultrasoft pseudopotentials to the projector augmented-wave method. *Phys. Rev. B,* 1999, **59** (3), 1758-1775.

4 J. Liu, Y. Gong, J. Wang, G. Peng, X. Miao, G. Xu, and F. Xu, Realization of zero thermal expansion in La(Fe,Si)13-based system with high mechanical stability. *Materials & Design,* 2018, **148**, 71-77.

5 N. Shi, X. Kong, A. Sanson, N. Wang, A. Venier, D. O. de Souza, and J. Chen, Observation of near-zero thermal expansion in $CrVMoO_7$. *Scripta Materialia,* 2023, **235**, 115597.

6 J. Xu, Z. Wang, H. Huang, Z. Li, X. Chi, D. Wang, J. Zhang, X. Zheng, J. Shen, W. Zhou; et al., Significant Zero Thermal Expansion Via Enhanced Magnetoelastic Coupling in Kagome Magnets. *Adv. Mater.,* 2023, **35** (8), 2208635.

7 J. C. Luo, K. X. Zou, B. Wang, X. L. Yuan, S. H. An, Z. J. Ma, K. W. Shi, S. H. Deng, J. P. Xu, W. Yin; et al., Zero Thermal Expansion Behavior in High-Entropy Anti-Perovskite $Mn_3Fe_{0.2}Co_{0.2}Ni_{0.2}Mn_{0.2}Cu_{0.2}N$. *Adv. Funct. Mate.,* 2024, **34** (52), 2140608.

8 H. Wang, M. Yang, M. Chao, J. Guo, Q. Gao, Y. Jiao, X. Tang, and E. Liang, Negative thermal expansion property of β-$Cu_2V_2O_7$. *Solid State Ionics,* 2019, **343**, 115086.

9 J. Hu, K. Lin, Y. Cao, C. Yu, W. Li, R. Huang, H. E. Fischer, K. Kato, Y. Song, J. Chen; et al., Adjustable Magnetic Phase Transition Inducing Unusual Zero Thermal Expansion in Cubic RCo2-Based Intermetallic Compounds (R = Rare Earth). *Inorg. Chem.,* 2019, **58** (9), 5401-5405.

10 G. Das Adhikary, P. Punetha, R. P. Singh, V. Dwij, V. Sathe, A. Senyshyn, P. Nukala, and R. Ranjan, Negative and zero thermal expansion in $K_{0.5}Bi_{0.5}TiO_3$. *Phys. Rev. B,* 2023, **108** (14), L140104.

11 T. Matsuda, J. E. Kim, K. Ohoyama, and Y. Moritomo, Universal thermal response of the Prussian blue lattice. *Phys. Rev. B,* 2009, **79** (17), 172302.

12 T. Chatterji, T. C. Hansen, M. Brunelli, and P. F. Henry, Negative thermal expansion of ReO3 in the extended temperature range. *Appl. Phys. Lett.,* 2009, **94** (24), 241902.

13 Y. Qiao, S. Zhang, P. Zhang, J. Guo, A. Sanson, X. Zhen, K. Zhao, Q. Gao, and J. Chen, Simple chemical synthesis and isotropic negative thermal expansion in $MHfF_6$ (M = Ca, Mn, Fe, and Co). *Nano Research,* 2024, **17** (3), 2195-2203.

14 A. E. Phillips, G. J. Halder, K. W. Chapman, A. L. Goodwin, and C. J. Kepert, Zero Thermal Expansion in a Flexible, Stable Framework: Tetramethylammonium Copper(I) Zinc(II) Cyanide. *J. Am. Chem. Soc,* 2010, **132** (1), 10-11.

15 Z. Jing-Ting, H. Yibole, B. Narsu, Z. Q. Ou, O. Haschuluu, O. Tegus, and F. Guillou, Structural and magnetic properties of Sc1-xNbxFe2 intermetallics showing anomalous zero thermal expansion. *Intermetallics,* 2021, **136**, 107252.

16 S. Dan, S. Mukherjee, C. Mazumdar, and R. Ranganathan, Zero thermal expansion with high Curie temperature in Ho2Fe16Cr alloy. *Rsc Adv,* 2016, **6** (97), 94809-94814.

17 K. Lin, W. Zhang, C. Yu, Q. Sun, Y. Cao, W. Li, S. Jiang, Q. Li, Q. Zhang, K. An; et al., Chemical heterogeneity modulated zero thermal expansion alloy over super-wide temperature range. *Cell Reports Physical Science,* 2023, **4** (2), 101254.

18 T. G. Amos. Negative thermal expansion in AOMO(4) compounds. Ph.D., Oregon State University, United States -- Oregon, 2000.